AMERICAN
METEOROLOGICAL
SOCIETY

Journal of Applied Meteorology and Climatology

EARLY ONLINE RELEASE

This is a preliminary PDF of the author-produced manuscript that has been peer-reviewed and accepted for publication. Since it is being posted so soon after acceptance, it has not yet been copyedited, formatted, or processed by AMS Publications. This preliminary version of the manuscript may be downloaded, distributed, and cited, but please be aware that there will be visual differences and possibly some content differences between this version and the final published version.

The DOI for this manuscript is doi: 10.1175/JAMC-D-16-0197.1

The final published version of this manuscript will replace the preliminary version at the above DOI once it is available.

If you would like to cite this EOR in a separate work, please use the following full citation:

Bringi, V., P. Kennedy, G. Huang, C. Kleinkort, M. Thurai, and B. Notaros, 2016: Dual-polarized radar and surface observations of a winter graupel shower with negative Zdr column. J. Appl. Meteor. Climatol. doi:10.1175/JAMC-D-16-0197.1, in press.

© 2016 American Meteorological Society

Manuscript (non-LaTeX)
Click here to download Manuscript (non-LaTeX) JAMC-D-16-0197_Revised_Manuscript.docx

Dual-Polarized Radar and Surface Observations of a Winter Graupel Shower with Negative Z_{dr} Column

***V. N. Bringi*[1], *P. C. Kennedy*[†2], *G.-J. Huang*[1], *C. Kleinkort*[1], *M. Thurai*[1], *B. M. Notaroš*[1]**

[1]Department of Electrical and Computer Engineering

Colorado State University, Fort Collins, CO, USA

[2]Department of Atmospheric Science

Colorado State University, Fort Collins, CO, USA

Submitted to **Journal of Applied Meteorology and Climatology**

26 May 2016

Revised: 12 September 2016

[†]Corresponding Author:
Patrick C. Kennedy
CSU-CHILL National Weather Radar Facility
30750 Weld County Road 45
Greeley, CO 80631, USA
Phone: (970) 491-6248 ex 202
E-mail: Patrick.Kennedy@colostate.edu

PRELIMINARY ACCEPTED VERSION

Abstract

Comprehensive analysis of an unusual graupel shower event recorded by an S-band polarimetric radar and two optical imaging surface instruments is presented. The primary radar characteristic was negative differential reflectivity, Z_{dr}, values along a vertical column. During the afternoon hours of 16 February 2015, a sequence of three showers composed primarily of small (8–15 mm diameter) graupel affected the ground instrumentation site that was established for the Multi-Angle Snowflake Camera and Radar (MASCRAD) experiment in the high plains region of Colorado. While these showers passed the instrumentation site, the CSU-CHILL radar conducted high time resolution (~2.5 minute cycle time) Range Height Indicator (RHI) scans from a range of 13 km. The RHI data show that the negative Z_{dr} values extended vertically through much of the reflectivity cores, implying that the reflectivity-weighted mean axis ratios of the graupel particles in this event remained somewhat prolate throughout their lifetime. Specifically, the convective shower cores only extended to heights of ~ 3.5 km AGL and had fractionally negative (~ −0.3 to −0.7 dB) Z_{dr} levels in the cores. Particle image data obtained by the MASC camera system and by a co-located 2D video disdrometer measured the diameters, shapes, and fall speeds of the graupel particles as they reached the surface. The graupel particles were found to be primarily of the lump type with a slightly prolate mean shape (especially for the larger diameter particles). Microwave backscatter calculations confirm that the graupel particle shape and orientation characteristics are consistent with the observed slightly, but consistently, negative Z_{dr} values.

1. Introduction

1.1 Overview

The Multi-Angle Snowflake Camera and Radar project (MASCRAD) was designed to characterize the microphysics of winter precipitation and modeling of associated polarimetric radar observables, with a longer-term goal to significantly improve radar-based quantitative precipitation estimation (or QPE) (Notaros et al. 2015). To support this effort, two optical instruments capable of making detailed observations of individual hydrometeors, a two-dimensional video disdrometer, (Schönhuber 2008), and a multi-angle snowflake camera (Garrett et al. 2012), were installed at a site located 13 km south-southeast of the CSU-CHILL radar in northeastern Colorado. To provide a reference for these hydrometeor observations, dedicated CSU-CHILL radar scans were conducted over the surface instrumentation site when precipitation was in progress. One event of particular interest during the MASCRAD observational campaign was the occurrence of several graupel showers that affected the surface instrumentation site during the afternoon hours of 16 February 2015 (Bringi et al., 2015; Kennedy et al. 2015). The surface hydrometeor observations showed that these showers were primarily composed of irregularly shaped graupel particles, while the radar detected fractionally negative differential reflectivity, Z_{dr}, values in the graupel shower echo cores.

In this paper, we relate the time evolution of the hydrometeor physical characteristics as derived from the optical instrument data to the dual polarization radar data collected in the immediate vicinity of the optical sensors. The paper is organized as follows: Section 1 continues with background information on the formation processes and structural characteristics of graupel. Section 2 describes the MASCRAD project instrumentation and gives an overview of the 16 February 2015 event in terms of the synoptic meteorological setting and the radar echo evolution. Section 3 describes observations at the Easton site and presents details of the graupel shower hydrometeor characteristics and analysis of measured data. Section 4 provides estimations of the axis ratio and dielectric constant of recorded particles and scattering computations in comparison with radar measurements. Finally, conclusions are offered in Section 5.

1.2 Graupel formation and dual polarization radar characteristics

It has been recognized for some time that graupel particles are the outcome of rime accumulations that are heavy enough to obscure the original embryo particle (Knight and Knight 1973). Laboratory measurements (Cober and List 1993) have shown that the density of the rime deposit varies with the rate at which supercooled droplets impact the collecting graupel particle, the size distribution of the impacting supercooled drops, and the graupel surface temperature. The measured rime density values were generally between 0.2 and 0.4 g cm^{-3} in these experiments (Cober and List 1993). Naturally-occurring graupel particle shapes have been classified into hexagonal, conical, or irregular lump categories (Magono and Lee 1966). Wind tunnel studies have shown that the conical shape begins as the expanding rime deposit accumulates on the upwind (lower) surface of the growing particle (Pflaum et al. 1978). Pflaum et al. (1978) also noted that slight asymmetries in the graupel particle's surface roughness, mass accumulation, etc. frequently induced pendulum-swing type motions. Rime collected during this swinging motion regime yields a conical particle shape. The final diameters of the graupel particles grown in this wind tunnel study averaged 1.1 mm. At larger diameters and higher terminal velocities (Reynolds numbers above ~500), the orientations of ~2 cm diameter conically-shaped plastic graupel replicas falling through a liquid bath were observed to be more unstable with quasi-random tumbling motions becoming preferred (List and Schumeneaur, 1971). Rime deposition during such tumbling particle motions leads to more spherical particle shapes.

These graupel density, shape and orientation variations significantly affect the particle's microwave backscatter properties. Dry, low density rime composition will reduce the bulk complex dielectric constant, making the particle's shape properties less apparent in dual-polarization radar measurements (Aydin and Seliga 1984). The size of the apex angle in conical graupel particles controls the maximum dimensions in the horizontal and vertical directions and variations in the ratio of the vertical to horizontal dimensions (or, loosely termed as axis ratio) can alter the sign of Z_{dr}. The scattering calculations of Evaristo et al. (2013) show that positive Z_{dr} develops as the apex angle becomes larger than ~50° – 70° depending upon the assumed particle geometry. At smaller apex angles, the axis ratio (ratio of maximum vertical dimension to maximum horizontal dimension) > 1 or prolate-like shapes, resulting in negative Z_{dr} whereas spherical particle shapes produce Z_{dr} of 0 dB. Oue et al. (2015) report on negative Z_{dr} as well as negative specific differential phase, K_{dp}, from X-band polarimetric radar which were ascribed to conical graupel formed in Arctic mixed phase clouds but did not provide in-situ verification.

Dual-polarization radar hydrometeor classification schemes generally associate graupel with reflectivity levels between 20 and 50 dBZ and differential reflectivity levels between −0.5 and + (1 to 2) dB (Liu and Chandrasekar 2000, and Straka et al. 2000). Most of these broad radar parameter ranges are due to variations in the shape and effective density of the graupel particles (for Z_{dr}) as well as the particle size distribution (PSD) (for horizontal reflectivity, Z_h). Here, measurements of the PSD along with the axis ratio from two orthogonal views are utilized along with estimation of density (via fall speed measurements and Böhm's methodology (Böhm 1989, and Huang et al. 2015) to compute Z_h and Z_{dr} for comparison with direct radar measurements of the same. This approach is expected to provide a more realistic method of comparing radar-measured variations in the (Z_h, Z_{dr})-plane with scattering calculations. Some earlier scattering studies assumed fixed conical shapes and particle densities to explain the negative Z_{dr} signature observed by radar (Evaristo et al. 2013, and Oue et al. 2015).

2. 16 February 2015 graupel shower observations

2.1 MASCRAD project instrumentation

The MASCRAD ground instrumentation site was established on the grounds of a small agricultural aviation airport (Easton Valley View) located at a range of 13.03 km on the 171.3° azimuth of the CSU-CHILL radar (Fig. 1) (Notaros et al. 2015; Kennedy et al. 2015). A site at relatively close range was desired to reduce the vertical separation between the center of the radar beam and the underlying ground surface. This effort was advanced by the ~30 m greater terrain height at the Easton site versus the CSU-CHILL location. The lowest antenna elevation angle that was free of ground clutter contamination at Easton was 1.5°. At this elevation angle the CSU-CHILL main beam was located between the heights of ~192 and 420 m AGL over Easton.

To reduce the effects of surface winds on the collection efficiency of the surface instruments, a two-thirds scale (8 m diameter) double fence intercomparison reference (DFIR) wind screen was constructed at the Easton site. The DFIR enclosure housed a Pluvio model 200 precipitation gauge and a surface mesonet station (measuring wind speed and direction, free air temperature, dew point, and atmospheric pressure) that was supplied by the National Center for Atmospheric Research (NCAR). NCAR also installed mobile sounding equipment that allowed radiosondes to be launched from Easton during periods of intensive observations. The NCAR S-Pol radar located ~33 km southwest of Easton documented larger scale radar echo patterns during the MASCRAD project. A summary of the CSU-CHILL radar operating characteristics is given in Table 1.

In addition to the sensors described above, two optical hydrometeor-sensing instruments, a two dimensional video disdrometer (2DVD) and a multi-angle snowflake camera (MASC), were also installed at the Easton site. The primary function of these optical instruments was to provide data to develop detailed three dimensional representations of the individual hydrometeor's ice / air structures to support microwave scattering calculations. Since the 3D particle reconstructions are not the primary thrusts of this paper, only a general overview of the observations provided by these optical instruments is given.

Of the two optical hydrometeor instruments installed at Easton, the 2DVD has a longer history of usage. The 2DVD used in the MASCRAD project was a low profile, third generation version of the instrument (Schönhuber 2008). The 2DVD generates two horizontal planes of visible light that are focused on line scan cameras composed of linear arrays of 625 active pixels and horizontal resolution of 160 μm (Fig. 2). Hydrometeors falling through the light beams shadow the individual diodes; the shadowing status of the diode arrays is recorded at a 55.17 kHz sampling rate. The two camera planes are perpendicular to each other, allowing two orthogonal silhouette views of the particles to be constructed. The camera planes are separated in the vertical by a calibrated distance of ~6.2 mm. Particle fall speeds are calculated from the time difference between the shadowing of the upper and lower light beams. The vertical resolution depends on the fall speed and is 100 μm for a 5 ms^{-1} fall speed. The virtual sampling area of the 2DVD is ~10 cm × 10 cm.

The multi-angle snowflake camera (MASC) was more recently developed at the University of Utah (Garrett et al. 2012). The basic MASC design uses three identical digital cameras mounted in a common horizontal plane with viewing angles that are separated by 36° (Fig. 3a). Two infrared motion detection beams with a vertical separation of 32 mm are located immediately above the common imaging volume of the cameras. Falling hydrometeors interrupt the IR beams, triggering both a bank of LED flash lamps as well as the cameras. Particle fall speeds are calculated based on the time delay between the interruptions in the upper and lower IR beams. The camera and lens equipment used in the CSU MASC produces 2448 × 2048 pixel grayscale images with a resolution of 35 μm per pixel.

To improve the 3D particle reconstructions (Kleinkort et al. 2015), two additional lower resolution (1288 × 964 pixel) cameras with a downward-looking view into the sample volume were added (Fig. 3b). The MASC horizontal sampling area is appreciably smaller than that of the 2DVD (~3 cm × 10 cm vs. 10 cm × 10 cm).

2.2 Synoptic setting and radar data summary

The 16 February 2015 graupel shower activity in the MASCRAD project area took place during a general regime of northwesterly flow at the 500 hPa level. At 12 UTC on 15 February, a short wavelength trough containing 500 hPa temperatures in the −25 to −27°C range was analyzed over western Montana and central Idaho. The general project forecast expectations were that periods of fairly widespread light to moderate snow would occur during the afternoon and overnight hours of Sunday, 15 February through the early morning of Monday, 16 February as the shortwave trough and associated surface cold front crossed the area. Coordinated S-Pol and CSU-CHILL data collection took place between ~19 UTC on the 15th through ~16 UTC on the 16th. Three NCAR MGAUS (mobile GPS advanced upper-air system) soundings were launched from Easton between 05 and 13 UTC on the 16th. Formal MASCRAD operations ended around 16 UTC on the 16th as most of the synoptic scale lift associated with the shortwave had moved south of the region. Overnight snow accumulations of ~25–75 mm were recorded in the Rocky Mountain foothills 40–60 km west of the CSU-CHILL radar. The immediate Easton area only received ~12 mm of snow.

In the wake of the nocturnal shortwave trough passage, the tropopause level in the 13 UTC Easton sounding had lowered to ~350 hPa (~6.5 km AGL; Fig. 4a). The NWS 12 UTC constant pressure level analyses at the 700 and 500 hPa levels (not shown) indicated that cold air advection was occurring in the MASCRAD project area. This is consistent with the overall backing wind directions that were observed between the surface and ~400 hPa in the Easton sounding. Early morning forecast discussions issued by the NWS Denver-Boulder office noted the possibility of mid-day shower development as surface heating in conjunction with the cold air advection aloft acted to promote steep lapse rates. This synoptic setting is quite similar to that described in an examination of two graupel shower events in (Evaristo et al. 2013). Fig. 5 shows the NWS sounding from one of the Evaristo el al. (2013) cases when conical graupel was observed at Lexington, MA. As in the Easton sounding, the close proximity of a mid-tropospheric low pressure system resulted in a low tropopause height that surmounted a surface-based moist layer containing relatively steep lapse rates. The Evaristo et al. study linked surface heating in this synoptic environment to the development of low-topped convective showers that were observed to produce small (~8 mm diameter) conical graupel at the ground.

Visibly growing cumulus clouds, some with opaque precipitation shafts, were first observed from the CSU-CHILL radar site at approximately 18:10 UTC on 16 February 2015. At

18:26 UTC, these initial shower echoes, with maximum low elevation reflectivity levels of 30 – 35 dBZ, were located along an axis that curved to the south and west of the Easton site (Fig. 6).

The vertical structure of one of the more intense echo cores centered 28 km west of CSU-CHILL was sampled in an RHI scan at 18:36 UTC (Fig. 7a). The convective echoes were shallow with the 0 dBZ reflectivity level reaching a maximum height of only ~ 3.5 km AGL. This height was nearly 2 km less than the depth of the moist layer in the 13 UTC Easton sounding (Fig. 4a). The vertical echo development may have been restrained by the slightly more stable lapse rates near the ~600 hPa level in the Easton sounding (Fig. 4b). The reflectivity cores in this RHI scan were consistently associated with negative Z_{dr} values in the −0.5 to −0.2 dB range (Fig. 7b). Within the > 21 dBZ regions of these echo cores, a localized Z_{dr} minimum sometimes occurred near the 3.5 – 4.0 km MSL (2.1 to 2.6 km AGL) height layer. These CSU-CHILL Z_{dr} values incorporate an adjustment to correct the −0.2 dB bias that was quantified using vertically pointed data obtained during a heavy snow event that occurred five days later. As an additional check on the CSU-CHILL Z_{dr} calibration, comparisons of the CHILL and S-Pol Z_{dr} values observed over the Easton site were done for the 03–08 UTC period on 16 February 2015 when the weakening precipitation echoes were still of usable strength. These comparisons indicated the CSU-CHILL Z_{dr} values had a maximum uncertainty of less than ~0.05 dB (see the Appendix for details). Finally, the Z_{dr} data recorded by the NWS KFTG radar located near Denver (roughly 60 km south of the echo band shown in Fig. 6) also contained fractionally negative Z_{dr} values in the high reflectivity areas of these showers. Negative Z_{dr} regions have been noted in the upper portions of thunderstorms where strong electric fields act to rotate the major axes of ice crystals towards the vertical (Hubbert et al, 2014). The Northern Colorado Lightning Mapping Array is located in the immediate CSU-CHILL area; this technology has demonstrated good sensitivity in the detection and 3D mapping of the VHF signals generated by various lightning phenomena (stepped leaders, etc.; Thomas et al., 2004). The Northern Colorado LMA network did not detect any discharges during the afternoon hours of 16 February 2016. Based on this, we suspect that cloud electrification played a minimal role in producing the observed negative Z_{dr} patterns.

The cellular nature of the precipitation echoes that developed during the afternoon hours of 16 February 2015 implied that graupel production was localized. To take advantage of an observing network with higher density than that provided by the NWS surface observation, the reports filed by the Community Collaborative Rain, Hail, and Snow (CoCoRaHS) network were examined. These observers routinely file precipitation totals recorded over 24 hour intervals. They also are encouraged to enter remarks describing notable precipitation characteristics, such as the occurrence of graupel. A total of 140 reports were filed from Larimer and Weld counties in Colorado (i.e., the immediate MASCRAD project area). The remarks section in five of these reports mentioned observations of graupel. The data archive for the Meteorological Phenomena Identification Near the Ground (mPING) was also examined for the local afternoon hours of 16 February 2015. This archive contained six reports mentioning either graupel or ice pellets. The locations of the four graupel reports (all from CoCoRaHs) within the geographical domain of Fig. 6 are marked with orange/red dots. Three of these reports were in the vicinity of the convective echo with the negative Z_{dr} core characteristics shown in Fig. 6.

3. Observations at the Easton site and detailed analysis of measured data

Three consecutive, but separate, showers were recorded at the Easton site, from (i) 19:30–19:34, (ii) 19:38–19:42, and (iii) 19:58–20:05 UTC. As these showers began to affect the

Easton site, repeated RHI scans with a cycle time of ~2.25 minutes were started. Figs. 8–10 show a sample of the echo evolution as period (i) began; similar evolution was also observed during periods (ii) and (iii). The RHI data showed a repeated tendency for echo development to initially occur aloft in the 2–3 km AGL height interval. These reflectivity cores typically contained an elevated echo maximum that remained near 2 km AGL. Narrow curtains of enhanced reflectivity developed downwards from these elevated cores and reached the surface within ~3–5 minutes. The majority of these developing/descending higher reflectivity cores were characterized by negative Z_{dr} values on the order of −0.5 to −0.2 dB.

3.1 Analysis of period (i) from 19:30–19:34 UTC

Fig. 11 shows the vertical profile of radar data at 19:32 UTC over the Easton site. At this time, the reflectivity near the surface was ~25 dBZ and more or less uniform with height up to 2 km; it then decreased rapidly to 0 dBZ at echo top. On the other hand, Z_{dr} was noted to be uniform at −0.2 dB below 2 km to surface, and rapidly increasing with height from 2 km upward to 0.8 dB at 3.5 km height where the sounding temperature was −26°C (see Fig. 4b). Such a vertical profile is suggestive of graupel particles below 2 km which originated via riming of the pristine crystals that were probably the predominant particle type in the higher-altitude positive Z_{dr} region.

Fig. 12 shows a sample image recorded by one of the 2DVD cameras at 19:30:08 UTC. The equi-volume diameter was 3.5 mm and the measured fall speed was 2.6 ms^{-1}. These quantities are typical values for small diameter graupel. Correspondingly, a sample image of the MASC cameras is shown in Fig. 13 at 19:30:18 UTC. The MASC-derived diameter (4.3 mm) and fall speed (2.6 ms^{-1}) are in good agreement with the 2DVD observations.

The mean vertical velocity versus diameter from the 2DVD for period (i) from 19:30–19:34 UTC is shown in Fig. 14. The equi-volume diameter (*D*) and fall speed are obtained by processing the raw line scan data from the two orthogonal cameras as described in Huang et al. (2015). Here, the mean fall speed in discrete bins of *D* is shown (with the +/−1σ bars) along with an exponential-type fit to the mean fall speed (dashed line). The fit to the mean fall speed versus *D* is representative of typical graupel reported in the literature (e.g., Locatelli and Hobbs 1974). A better fit to the observations was obtained by using an exponential relationship versus a power law.

The hydrometeor size distributions for each of the three shower periods were developed using the methods of Huang et al. (2015) as applied to the 2DVD data (Fig. 15). Clearly, sampling issues are evident for the larger sizes with $D > 5$ mm (mainly for period *ii* discussed below) but the shape is reasonably close to exponential for $0.5 < D < 3$ mm with different slopes and intercept parameters.

3.2 Analysis of period (ii) from 19:38–19:42 UTC

The second shower occurred between 19:38–19:42 UTC. The associated vertical profiles of Z_h and Z_{dr} over Easton are shown in Fig. 16.

While the general features of the vertical profiles shown in Figs. 11 and 16 are similar, the 2DVD data showed a mix of smaller graupel and larger aggregate particles during the later (19:38–19:42 UTC) period. The largest particle recorded by the 2DVD at 19:41:24 UTC is shown in Fig. 17 and seen to be clearly an aggregate (apparent *D* of 8.2 mm and measured fall speed of 1.3 ms^{-1}).

An example MASC image of one of these large aggregates observed at 19:41:32 UTC is shown in Fig. 18. This particle's diameter and measured fall speed were 5.6 mm and 1.5 m^{-1}, respectively. Evidence of this aggregate's complex structure and moderate degree of riming are also apparent in Fig. 18.

The distribution of the hydrometeor vertical velocities obtained from the 2DVD measurements during the 19:38–19:42 UTC period is shown in Fig. 19. This distribution clearly shows a population of both faster-falling graupel (D < 2 mm) and slower, higher drag coefficient snow aggregates (D > 2 mm). The plotted points are the fall speeds for each individual particle and no fit is attempted for the mixture. Visually, a power law fit is possible for D < 1 mm with more or less constant fall speed of 1.5 m/s being characteristic of the aggregates with D > 2 mm. The latter fall speed is typical for aggregates of dendrites (Brandes et al. 2008). The particle size distribution averaged over this same four minute period (19:38–19:42 UTC) is shown in Fig. 20. This distribution is consistent with a mixture of smaller graupel (D < 2 mm) with larger snow aggregates (D > 3 mm with maximum of 8 mm).

4. Scattering simulations and comparisons with radar measurements

4.1 Estimation of the height/width ratio of particles from 2DVD images

To understand the origin of the observed weak negative Z_{dr} signatures we have used the 2DVD images to estimate the height-to-width ratio (h/w) for all the particles recorded for the three periods as a function of D. Fig. 21 illustrates the dimensions (h and w) obtained from the vertical 'stack' of line scans from one camera. The height is simply the vertical velocity multiplied by the total time needed to complete the stack of line scans, which is not dependent on the horizontal movement of the particle. The width is taken as the maximum line scan dimension in the stack which is also not dependent on horizontal movement (in the presence of horizontal movement, the line scans are shifted horizontally so the stack appears skewed but the maximum line scan dimension is not altered). A similar height-to-width ratio is performed for the orthogonal camera image and the final h/w is computed as the geometric mean of the two camera measurements.

One can loosely refer to h/w ratio as the axis ratio of an equivalent spheroid (prolate if $h/w > 1$ and oblate if $h/w < 1$). Fig. 22 shows the results in terms of bin averaged mean and +/−1σ bars of the axis ratio (i.e., averaged over bins of D). While there is substantial scatter in the axis ratios, the fit to the mean axis ratios shows oblate-like shapes for $D < 1$ mm and weak prolate-like shapes for $D > 2$ mm. One can consider this as a bulk axis ratio versus D relation for this data set (encompassing all three periods over Easton site). It is clear that the mean axis ratio is prolate-like when $D > 1$ mm, whereas it is oblate-like for $D < 1$ mm. For Rayleigh scattering, the corresponding single particle Z_{dr} will be, correspondingly, negative and positive (in dB units). While the graupel shape varies considerably, the details of the shape are less important in determining the Z_{dr} as opposed to whether the gross shape is oblate-like (positive Z_{dr}) or prolate-like (negative Z_{dr}).

4.2 Dielectric constant estimation and T-matrix scattering calculations vs. radar data

To complete the scattering model (Mishchenko 2014) (given the size distribution and the axis ratio versus D), the particle density must be estimated from which the dielectric constant can be calculated using Maxwell-Garnet mixing formula (ice-air two component mixture). The methodology for computing the density follows Böhm (1989) and is adapted for 2DVD data by Huang et al. (2015) which is used herein. In brief, from the terminal fall speed, area ratio (ratio of shadowed pixel area to minimum circumscribed ellipse), apparent *D* and environmental parameters, the mass is calculated for each particle (the error in derived particle mass has been estimated by Szyrmer and Zawadzki 2010 to be around 40-50%). Since the apparent volume is computed from the two orthogonal stacks, the density follows as the ratio of mass to volume. Finally, a power law fit to the mean density versus *D* is performed for the entire period (Fig. 23; the dielectric constant follows directly). The mean density for each period is also computed as the ratio of the mean mass to the mean volume. For the three periods they are, respectively, 0.18, 0.06, and 0.19 g cm^{-3}, respectively. The lower value obtained during period (ii) reflects the presence of large aggregates. The densities so computed appear to be on the low side relative to the literature (Pruppacher and Klett 2010). However, as demonstrated below, the computed reflectivity would be too large as compared with the radar measurements if *ad hoc* assumption of fixed graupel density from the literature were assumed (≈ 0.5–0.7 g/cc).

The size distribution averaged over each of the three periods, axis ratio versus *D* and dielectric constant are input to the T-matrix scattering code which computes radar reflectivity (Z_h) and Z_{dr} at S-band (note: the spheroids are assumed to be oriented with symmetry axis vertical). Fig. 24 shows the scatterplot of Z_{dr} versus Z_h from the radar data for the three periods. The radar data are averages obtained from the RHI scans at 1932, 1940 and 2000 UTC and in the 0.5 – 1.0 km AGL height interval (ranges are ±5 km centered at Easton site). As noted in Section 2.2, the calibration of the Z_{dr} values has been validated using the procedures described in the Appendix. Overlaid are the results from the scattering model assuming (1) mean density within each period, (2) density versus *D* fit to the combined data from all three periods, and (3) assuming fixed particle densities of 0.2 and 0.4 g cm^{-3}. The dielectric constant of dry graupel particles is computed using the Maxwell-Garnet mixing formula for a two-phase mixture of ice and air. The dielectric factor $|K_p|^2 = \rho_p^2\ |K_{ice}|^2$ where $|K_{ice}|^2$ is the dielectric factor of solid ice and ρ_p is the particle density. For each density model the lowest, intermediate and largest Z_h correspond, respectively, to periods (iii), (i) and (ii).

The trend from the scattering calculations shows weakly negative Z_{dr} (lower bound of −0.4 dB) independent of Z_h. For each density model described above, the lowest, intermediate and largest Z_h correspond, respectively to periods (iii), (i) and (ii) which is consistent with the occurrence of larger sizes in the respective N(D) (see Fig. 15). But the $|Z_{dr}|$ is relatively constant for each density model independent of Z_h.

The scatter from the different density assumptions falls within the scatter from the radar measurements though the radar Z_{dr} values span both positive and negative Z_{dr}. This is shown more clearly in Fig. 25, depicting the histogram of radar measured Z_{dr}, which is skewed to negative values. Overall, the scattering simulations using 2DVD-derived parameters of the variation of Z_{dr} versus Z_h capture the weak trend towards negative Z_{dr} that was observed by radar.

4.3 Analysis of LDR radar measurements from RHI scans over Easton

Finally, Fig. 26 shows a scatterplot of the linear depolarization ratio (LDR: trasmit H and receive V) versus reflectivity (at H-polarization) to illustrate the range of LDR in the winter graupel example. The radar is capable of measuring LDR values as low as −40 to −43 dB (Bringi et al. 2011). The LDR system bias was corrected using solar scans (Brunkow et al. 2000). To avoid noise biasing the LDR measurement, the data shown in Fig. 26 were selected with the crosspolar SNR (signal to noise ratio) > 5 dB. Note that the radar data were collected using alternate pulsing of the H and V transmitters with PRT of 0.5 msec. The high speed transfer switch (after the low noise amplifiers) was exercised to route the copolar (i.e., HH and VV) signals to one receiver and the crosspolar (i.e., VH and HV) signals to the second receiver (Brunkow et al. 2000).

While Z_{dr} is related to the reflectivity-weighted mean axis ratio of the backscattering particles within the radar pulse volume, the LDR is responsive to the presence of non-spherical, relatively high dielectric particles that are oriented at appreciable angles to the incident H polarized radar waves. Since the graupel particles observed in this case had only modest departures from spherical shapes and were composed of low bulk density ice, LDR are expected to be small (i.e., below the ~ −26 dB values associated with large raindrops; Bringi and Chandrasekar 2001). The LDR values from the graupel showers range from −36 to −29 dB with average around −32 dB, independent of reflectivity. In general, the LDR will vary with particle density, canting angle, and axis ratio distributions, and less so with reflectivity (excluding the rain case where the mean axis ratio decreases with increasing size; Bringi and Chandrasekar 2001). As such, scattering simulations of LDR using bulk assumptions about particle density, canting angle, and shape cannot give the range of values obtained from direct measurements. Rather, a 'particle-by-particle' scattering simulation approach is needed (Thurai et al. 2009).

5. Conclusions

Graupel in this case was produced by low-topped convective cells whose development was promoted by cold mid-tropospheric temperatures (500 hPa environmental temperature of ~ −27°C). While no in-situ data are available, we surmise that the several meters per second updraft magnitudes that typically exist in the active regions of clouds of this type were strong enough to generate a supercooled liquid environment in which graupel particles grew by riming. Sub-freezing temperatures and relatively humid conditions between the mid-tropospheric and near-surface levels aided the survival of the graupel particles as they descended to the ground. The most distinctive dual polarization radar characteristic of these graupel showers was their slightly, but consistently, negative Z_{dr}. These graupel shower synoptic environment and radar characteristics are consistent with those found by Evaristo et al. (2013).

This study has provided more detailed observations in terms of high time resolution RHI scans of the parent convective echoes and physical characterizations of the individual graupel particles obtained from surface-based optical instruments. The RHI data showed that the negative Z_{dr} values extended vertically through much of the reflectivity cores. Within these echo cores, there was a tendency for slightly more negative Z_{dr} to occur in the 2.1 to 2.6 km AGL height region. Wind tunnel studies of "freely falling" graupel particles have shown that various swinging, pendulum type motions occur as rime accumulates on the bottom (upstream) surface of the particle (Pflaum et al. 1978). The resultant concial shapes tend to fall with the major axis oriented towards the vertical direction with the apex up (Ziknunda and Vali 1972), promoting negative Z_{dr} values. Graupel particles that reach larger diameters and higher Reynolds numbers have a greater tendency to develop tumbling motions that would result in $Z_{dr} \approx 0$ dB (List and Schemenaur 1971). We speculate that conical graupel shapes may have been more prevelant in the ~2.1–2.6 km AGL levels of the echo cores where Z_{dr} tended to be slightly more negative. Apparently the growth and reorientation process that were active during the particle's subsequent descent to the surface caused the graupel shapes to tend more towards the irregular lumps seen in the optical instrument images. The height-to-width ratio statistics calculated from the 2DVD data show that the primarily lump type graupel particles observed in this case still had a slightly prolate mean shape characteristic. Apparently, the growth-related transition to quasi-spherical graupel shapes, with a characteristic Z_{dr} of ~0 dB, was not completed in this event.

Three consecutive periods (each lasting ~ 4 minutes) of graupel showers were recorded by the 2DVD and the MASC at the Easton measurement site coordinated with high resolution radar RHI scans. The 2DVD measurements of fall speed and size were used to estimate the mean density for each period as well as the density versus size fit to data from all three periods using Böhm's (1989) methodology. The height-to-width ratio was determined for each particle and a mean fit of this ratio with size was obtained along with the average PSD for each period. The T-matrix method was used to calculate the reflectivity and Z_{dr} for each of the three periods under different density estimates including fixed density of 0.2 and 0.4 g cm^{-3}. The simulated Z_{dr} values were seen to be slightly negative depending on the density assumption, in agreement with the radar measurements from range resolution volumes above the Easton site (which encompassed both positive and negative Z_{dr} but with a distinct negative skewness in the histogram shape). The scatterplot of Z_h versus Z_{dr} from the simulations showed good agreement with the corresponding radar-based measurements. The density estimation was found to be an important factor in constraining both the simulated reflectivity and Z_{dr} values to fall within the radar-based values. LDR values generated by the lump-type graupel shapes in these showers averaged ~ −32 dB. This value is consistent with the slightly prolate particle axis ratios that were derived from the 2DVD statistics.

Acknowledgements

This work was supported by the National Science Foundation under Grant AGS-1344862. We also acknowledge Bob Easton, owner of the Easton Valley View Airport, for providing us the location for the MASCRAD Field Site, Walter Petersen, of NASA Wallops, for lending the 2DVD SN36 and PLUVIO200 to us for the MASCRAD snow season 2014/2015, Robert Bowie for off-hour CSU-CHILL radar operations, Andrew Newman, of the National Center for Atmospheric Research (NCAR) for project forecasting support, Timothy Lim and William Brown, of NCAR, for performing MGAUS soundings during the 2014/2015 MASCRAD winter campaign, and John Hubbert, of NCAR, for collaboration in running the NCAR SPOL radar observations.

APPENDIX

CSU-CHILL Radar Z_{dr} Calibration Verification

During the MASCRAD campaign, NCAR's S-Pol radar was also used to perform regular scans over Easton during significant events. Although the S-Pol radar did not operate during the time of the graupel event on 16 Feb 2015, it did however perform the (pre-defined) Easton schedule scans during a widespread snow event about 12 h earlier. As with the CHILL scan schedule, the S-Pol scans also included regular RHI scans over the Easton site. Fig. A1(a) shows the locations of the CHILL radar and the S-Pol radar (marked with solid black dots) as well as the directions of the RHI scans over Easton (black lines). While the Easton site was 13 km away from the CHILL radar, the range from the S-Pol radar site was 33 km along 45° azimuth. The hypothesis is that by comparing the Z_{dr} histograms from the two independently calibrated radars from a widespread snow event (albeit some 12 h earlier to the graupel event) will give strong credibility to the physical interpretation of the weak negative CHILL Z_{dr} measurements in the graupel event reported in this article. One caveat is that the two radars have different viewing angles of the snow but the Z_{dr} difference (in our case of aggregated low density snow) is expected to be negligible.

For S-Pol, the Z_{dr} offset was determined by the method described by Hubbert (private communication) which depends (among other factors) on the ambient temperature at the S-Pol radar site. The accuracy of the S-Pol Z_{dr} calibration using this technique (which was fine-tuned for the snow event) is expected to be within − +0.01 dB or better. In the case of CHILL Z_{dr} the calibration was obtained via analysis of vertical pointing (VP) data from another snow event 5 days later which was applied to the graupel case reported in this article and to the snow event reported in this Appendix.

The S-Pol and CHILL radar data over the Easton site were extracted from their corresponding RHI scans for a five hour period, viz., from 03:00 to 08:00 UTC on 16 Feb 2015. Fig. A1(b) compares the histograms of the respective Z_{dr} values over the 0.6–1.4 km height interval over the Easton site, with Z_h > 10 dBZ. The latter threshold was determined so as to ensure high SNR (> 10–15 dB for the S-Pol radar) and to minimize any differences due to somewhat different Z_{dr} noise correction procedures employed by the two radars. CHILL histograms are shown as grey dotted line, and the S-Pol shown as black solid line. As seen from Fig. A1(b), both the CHILL Z_{dr} histogram and the S-Pol Z_{dr} histogram are very close to each other. In order to quantify the differences between the two histograms, a non-linear least-squares fit to a Gaussian function $f(x)$ was performed for both cases, where $f(x)$ is given by:

$$f(x) = a_0 \mathrm{e}^{-(x-a_1)^2 / 2a_2^2} ,$$

where x represents Z_{dr} and $f(x)$ represents the percentage probability associated with the histograms. The closest visual agreement was obtained when an offset adjustment of +0.05 dB was added to CHILL Z_{dr} assuming that S-Pol serves as ‘truth’. The fitted curves are also included in Fig. A1(b), and as seen the two curves are very close to each other. The best-fit coefficients were:

CHILL: $a_0 = 11.0$ $a_1 = 0.35$ $a_2 = 0.34$

S-Pol: $a_0 = 10.6$ $a_1 = 0.36$ $a_2 = 0.37$

where a_0 represents maximum value of $f(x)$, and a_1 and a_2 are, respectively, the mean and standard deviation of x from the fitted Gaussian curves. Once again, they are numerically very close to each other. Thus, the CHILL Z_{dr} calibration adjustment appropriate for the snow time period of 03:00–08:00 UTC can be assumed to be +0.05 dB.

To account for possible small receiver front-end drifts (affecting bias in Z_{dr}) due to the warming trend from the snow event to the graupel event, we have made use of data from test pulses regularly injected at the receiver front-end inputs during operations and have determined that the relative change in the Z_{dr} drift due to the receiver front-ends only is a further −0.07 dB. The drift appears to be correlated with temperature change at the University of Northern Colorado (located ~7 km southwest of CSU-CHILL), as shown in Fig. A2(a) and (b). Thus, assuming there is no differential change in the passive H and V microwave paths (due to temperature change) from antenna feed to the test pulse injection plane, the best estimate for the Z_{dr} offset adjustment (over and above the VP-scan based calibration) during the graupel event is inferred to be −0.02 dB. To conclude, the Z_{dr} calibration as applied to the graupel event is expected to be accurate to within ±0.05 dB.

References

Aydin, K. and T.A. Seliga, 1984: Radar polarimetric backscattering properties of conical graupel. *J. Atmos. Sci*. **41**, 1887-1892.

Bohm, H.P., 1989: A general equation for the terminal fall speed of solid hydrometeors., *J. Atmos. Sci.*, **46**, 2419-2427.

Brandes, E.A., K. Ikeda, . Thompson, M. Schonhuber, 2008: Agggregate terminal velocity / temperature relations. *J. Appl. Meteo. Climo*., **47**, 2729-2736.

Bringi, V.N and V. Chandrasekar, 2001: *Polarimetric Doppler Weather Radar: Principles and Applications*. Cambridge University Press, 636 pp.

Bringi, V.N., R. Hoferer, D.A. Brunkow, R. Schwerdtfeger, V. Chandrasekar, S.A. Rutledge, J. George, and P.C. Kennedy, 2011: Design and performance characteristics of the new 8.5m dual-offset Gregorian antenna for the CSU-CHILL radar., *J. Atmos. Ocean. Tech*, **28**, 907-920.

Bringi, V. N., B. Notaros, C. Kleinkort, G.-J. Huang, M. Thurai, and P. Kennedy, 2015: Comprehensive Analysis of an Unusual Winter Graupel Shower Event Recorded by an S-Band Polarimetric Radar and Two Optical Imaging Surface Instruments. *American Meteorological Society's 37th Conference on Radar Meteorology*, 14-18 September, 2015, Norman, OK.

Brunkow, D.A., V.N. Bringi, P.C. Kennedy, S.A. Rutledge, V. Chandrasekar, E.A. Mueller, and R.K. Bowie, 2000: A description of the CSU-CHILL national radar facility., *J. Atmos., Ocean. Tech*, **17,** 1596-1608.

Cober, S.G. and R. List 1993: Measurements of the heat and mass transfer parameters characterizing conical graupel growth. *J. Atmos. Sci*, **50**, 1591-1609.

Evaristo, R., T. Bals-Esholz, E. Williams, A.J. Fenn, M. Donovan, and D. Smalley, 2013: Relationship of graupel shape to differential reflectivity: Theory and observations. AMS 29th Conference on Environmental Information Processing, Austin, TX, January 6 – 10, 2013.

Garrett, T. J., C. Fallgatter, K. Shkurko, and D. Howlett, 2012: Fall speed measurement and high-resolution multi-angle photography of hydrometeors in free fall. Atmospheric Measurement Techniques, 5, 2625-2633.

Huang, G.-J., V.N. Bringi, D. Moisseev, W.A. Petersen, L. Bliven, D. Hudak, 2015: Use of 2D-Video Disdrometer to Derive Mean Density-Size and Ze-SR Relations: Four Snow Cases from the Light Precipitation Validation Experiment. *Atmospheric Research*.

Hubbert, J. C., S. M. Ellis, W. Y. Chang, S. Rutledge, and M. Dixon, 2014: Modeling and interpretation of S-band ice crystal depolarization signatures from data obtained by simultaneously transmitted horizontally and vertically polarized fields. *J. Appl. Meteo. Climo*, **53**, 1659-1677.

Kennedy, P. C., C. Kleinkort, G.-J. Huang, M. Thurai, A. Newman, J. Hubbert, S. Rutledge, V. N. Bringi, and B. M. Notaros, 2015: Preliminary Results from the Multi-Angle Snowflake

Camera and Radar (MASCRAD) Project. *American Meteorological Society's 37th Conference on Radar Meteorology*, 14-18 September, 2015, Norman, OK.

Kleinkort, C., G.-J. Huang, E. Chobanyan, A. Manic, M. Ilic, A. Pezeshki, V. N. Bringi, and B. Notaros, 2015: Visual Hull Method Based Shape Reconstruction of Snowflakes from MASC Photographs. *Proceedings of the 2015 IEEE International Symposium on Antennas and Propagation and North American Radio Science Meeting*, July 19-25, 2015, Vancouver, BC, Canada.

Knight, C.A. and N. C. Knight, 1973: Conical graupel. *J. Atmos. Sci*., **30**, p.118-124.

List, R. and R.D. Schemenauer, 1971: Free-fall behavior of planar snow crystals, conical graupel and small hail., *J. Atmos. Sci*., **28**, 110-115.

Liu, H. and V. Chandrasekar, 2000: Classification of hydrometeors based on polarimetric radar measurements: Development of fuzzy logic and neuro-fuzzy systems and in-situ verification. *J. Atmos. Ocean. Tech*, **17**, 140-164.

Locatelli, J.D. and Hobbs, P.V., 1974: Fall speeds and masses of solid precipitation particles. *Journal of Geophysical Research*, **79**: 2185-2197.

Magono, C. and C. Lee, 1966: Meteorological classification of natural snow crystals. J. Fac. Sci. Hokkaido Univ. Ser. 7, 2, 321-335.

Mishchenko, M. I., 2014: *Electromagnetic Scattering by Particles and Particle Groups: An Introduction*. Cambridge University Press.

Notaros B., V. N. Bringi, C. Kleinkort, G.-J. Huang, E. Chobanyan, M. Thurai, O. Notaros, A. Manic, A. Newman, P. Kennedy, J. Hubbert, T. Lim, W. Brown, and M. Ilic, 2015: Measurement and Characterization of Winter Precipitation at MASCRAD Snow Field Site. *Proceedings of the 2015 IEEE International Symposium on Antennas and Propagation and North American Radio Science Meeting*, July 19-25, 2015, Vancouver, BC, Canada.

Oue, M., M.R. Kumjian, Y. Lu, Z. Jiang, E. Clothiaux, J. Verlinde, and K. Aydin, 2015: X-band polarimetric and Ka-band observations of a graupel-producing Artic mixed-phase cloud. *J. Appl. Meteor. Climo*, **54**, 1335-1351.

Pflaum, J.C., J.J. Martin, and H.R. Pruppacher, 1978: A wind tunnel investigation of the hydrodynamic behaviour of growing, freely falling graupel., *Quart, J. R. Met. Soc*., **104**, 179-187.

Pruppacher, H.R. and J.D. Klett, 2010: Microphysics of Clouds and Precipitation, Springer Netherlands, 954 pp.

Schönhuber, M., G. Lammer, and W. L. Randeu, 2008: The 2D-video-distrometer. Precipitation: Advances in Measurement, Estimation and Prediction, S. Michaelides, Ed., Springer, 3–31, doi:10.1007/978-3-540-77655-0_1.

Straka, J.M., D.S. Zrnic, and A.V. Ruzhkov, 2000: Bulk hydrometeor classification and quantification using polarimetric radar data: Synthesis of relations. *J. Appl. Meteor*., **39**, 1341-1372.

Thomas, R., P., P. R. Krehbiel, W. Rison, J. Hunyady, W. P. Winn, T. Hamlin, and J. Harlin, 2004: Accuracy of the lightning mapping array. *J. Geophys. Res*., **109**, D14207.

Thurai, M., V. N. Bringi, and W. A. Petersen, 2009: Rain microstructure retrievals using 2-D video disdrometer and C-band polarimetric radar. *Adv. Geosci*., vol. **20**, 13−18.

Zikmunda, J and G. Vali, 1972, Fall patterns and fall velocities of rimed ice particles, *J. Atmos, Sci*, 1334, 1347.

Tables

Table 1: CSU-CHILL radar characteristics in MASCRAD 2014/2015 winter campaign:

CSU-CHILL radar parameter	
Wavelength (cm)	11.0
3 dB beamwidth (deg)	1.0
Peak transmit power (KW)	430
Pulse repetition frequency (kHz)	2.0
Polarization mode	Alternating VH
Linear Depolarization Ratio measurement limit (dB)	~ -40
Range gate length (m)	150
Antenna elevation (m MSL)	1432

Figure Caption List

Figure 1. Locations of the primary observing sites used in the 2014/2015 MASCRAD operations. Horizontal distances are in km from the CSU-CHILL radar.

Figure 2. Schematic diagram of the two-dimensional video disdrometer (2DVD) (after Schönhuber et al. 2008).

Figure 3. (a) Schematic diagram of the basic multi-angle snowflake camera (MASC; Garrett et al 2012). Irregular yellow-shaded area indicates the region in which falling hydrometeors will trigger the lights and cameras. (b) The CSU MASC installation, including two additional externally added cameras, at the Easton site.

Figure 4. (a) Skew T-Log P plot of the data launched at 13:01 UTC on 16 February 2015 from the Easton site. Wind speeds plotted in m s^{-1}. (b) Magnified view of the lower, graupel shower-bearing, portion of the sounding shown in (a). For reference, the 700 hPa height (-12.5^{o} C) is at 1550 m AGL and the 500 hPa height (-30.6^{o} C) is at 4030 m AGL. The graupel shower echo top height was ~3.5 km AGL (see Figure 11). The sounding temperature at this height was -26^{o} C.

Figure 5. Skew T-Log P plot of the NWS sounding from Chatham, MA at 12 UTC on 12 April 2012. Showers producing small, conical graupel at the surface were observed later on this day (Evaristo et al. 2013).

Figure 6. Reflectivity data from the CSU-CHILL radar at 18:24 UTC on 16 February 2015. Elevation angle is 3°; axis labels are in km from an origin at the CSU-CHILL radar.

Figure 7. CSU-CHILL RHI scan reflectivity (a) and differential reflectivity (b) data on an azimuth of 261° at 18:35 UTC on 16 February 2015. For reference with panel (a), the solid blue contours in panel (b) are 21 and 27 dBZ.

Figure 8. (a) CSU-CHILL RHI scan data taken on the azimuth of the Easton site (171°) at 19:26:43 UTC on 16 February 2015. Easton is located essentially at the 13 km range mark. (a) Z_h in dBZ. (b) Z_{dr} in dB. Solid blue contour lines are 21 and 27 dBZ.

Figure 9. As in Fig. 8 but for the volume start time at 19:29:20 UTC (on 16 February 2015).

Figure 10. As in Fig. 8 but for the volume start time at 19:31:57 UTC.

Figure 11. Height profiles of Z_h (blue) and Z_{dr} (red) averaged over a range interval of ± 0.25 km of the Easton site at 19:32 UTC on 16 February 2015. Temperatures (ºC) from the 13 UTC Easton sounding are indicated on the abscissa at height intervals of 0.5 km. Temperatures from the 00 UTC NWS Denver sounding are also given. Note that above height of 3.8 km the Z_{dr} data were classified as being due to "non-meteo" echoes and should be disregarded.

Figure 12. Sample graupel image from one camera of the 2DVD collected at 19:30:08 UTC (on 16 February 2015) at the Easton site. The equi-volume spherical *D* is 3.5 mm using the images from both cameras. The measured fall speed was 2.6 m/s.

Figure 13. Sample graupel image from one camera of the MASC (in Fig. 3b) at 19:30:18 UTC. Via 3D reconstruction using five images, the equi-volume spherical *D* is 4.3 mm and fall speed was observed to be 2.6 m/s.

Figure 14. The bin-averaged vertical velocity versus equi-volume diameter (*D*) from the 2DVD for period (i) (19:30-19:34 UTC, on 16 February 2015). The +/− 1σ bars are shown along with an exponential fit (dashed blue line). The power law fit is shown by the dashed red line. The hydrometeors were predominantly small graupel during this time period.

Figure 15. Hydrometeor size distribution *N* versus *D* for the three precipitation shower events. The presence of larger diameter snow aggregates is apparent during period (ii) (plotted in black). The total number of particles sampled during periods (i), (ii) and (iii) were, respectively, 1917, 619 and 513.

Figure 16. As in Fig. 11 but for 19:40 UTC (shower event period (ii)).

Figure 17. Sample 2DVD image of a large aggregate (*D* = 8.2 mm; fall speed: 1.3 m/s) at 19:41:24 UTC.

Figure 18. Sample MASC image of a large aggregate (D = 5.6 mm; fall speed: 1.5 m/s) at 19:41:32 UTC.

Figure 19. Scatterplot of the vertical velocity versus D from the 2DVD for period (ii) (19:38–19:42 UTC).

Figure 20. Particle size distribution $N(D)$ for period (ii).

Figure 21. Example of the estimation of height (h) and width (w) from a sample single-camera 2DVD image. The h/w ratio is here loosely referred to as 'axis ratio'.

Figure 22. Plot of the bin averaged mean of the height/width versus D from the 2DVD for the entire graupel shower period. Bars depict the $+/-1\sigma$ extent of the axis ratio values in each diameter bin. Mean fit is shown as blue solid line. Dashed line represents height/width = 1.

Figure 23. Hydrometeor bulk density vs. diameter for the entire observation period. Vertical bars indicate +/- 1 σ range around the mean value in each diameter bin. Red line is 5th order polynomial fit to the observations: note that we assume $\rho(D>2.875 \text{ mm}) = \rho(D=2.875 \text{ mm})$ for the polynomial fit. Green dashed line is the fitted power law density versus diameter relationship.

Figure 24. Z_{dr} versus Z_h from radar measurements for all three time periods compared with scattering simulations based on the $N(D)$, mean axis ratio, and density from the 2DVD (various

density models are as indicated in the legend). For each density model the lowest, intermediate and largest Z_h correspond, respectively, to periods (iii), (i) and (ii).

Figure 25. Histogram of radar measured Z_{dr} from all RHI scans over the Easton site from 19:34–20:11 UTC. Data selected from the range interval 10–22 km (range to the Easton site is ~13 km) and height interval 0.5–1.0 km (AGL).

Figure 26. Scatterplot of LDR versus reflectivity radar measurements from RHI scans over Easton. Data selected from the range interval between 10 and 22 km and height interval between 0.5 and 3.0 km (AGL). Bin averaged LDR is also shown along with +/−1σ bars.

Figure A1. (a) Depiction of the locations of the CSU-CHILL and NCAR S-Pol radars relative to the Easton instrumentation site. (b) Histograms of Zdr data in the immediate Easton area during widespread snow in the 03 – 08 UTC period on 16 February 2015. S-Pol data plotted in black and CSU-CHILL data in grey.

Figure A2. (a) Difference in dB of the test pulse signal levels recorded in the H and V receiver channels of the CSU-CHILL radar as a function of time on 16 February 2015. (Note: The data gap in the 17 – 18 UTC period occurred when the radar was put into standby mode to await echo development). (b) Ambient air temperature measurements for the same time period as recorded at the University of Northern Colorado Earth Science Department. This measurement site is approximately 7 km southwest of the CSU-CHILL radar.

Figures

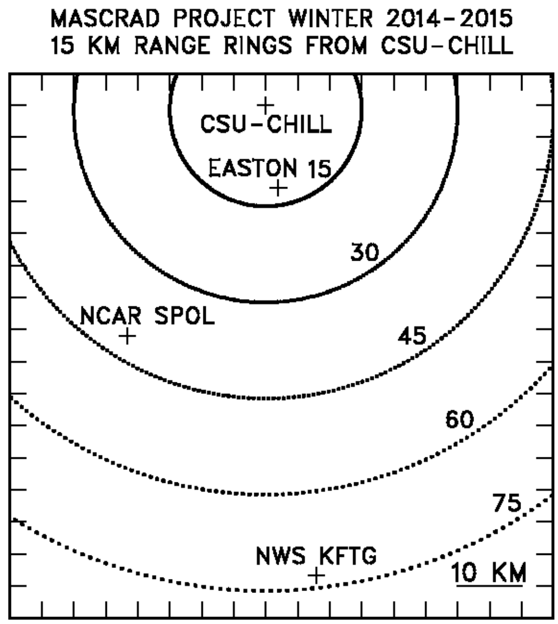

Figure 1. Locations of the primary observing sites used in the 2014/2015 MASCRAD operations. Horizontal distances are in km from the CSU-CHILL radar.

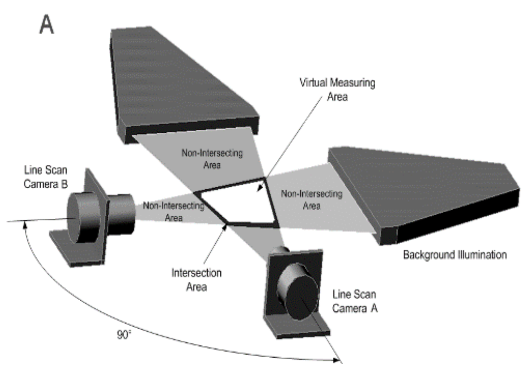

Figure 2. Schematic diagram of the two-dimensional video disdrometer (2DVD) (after Schönhuber et al. 2008).

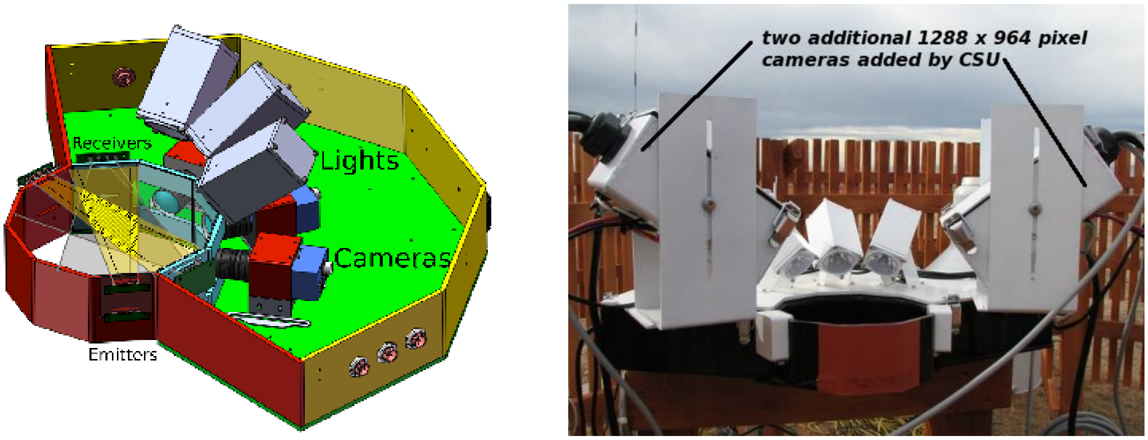

(a) (b)

Figure 3. (a) Schematic diagram of the basic multi-angle snowflake camera (MASC; Garrett et al 2012). Irregular yellow-shaded area indicates the region in which falling hydrometeors will trigger the lights and cameras. (b) The CSU MASC installation, including two additional externally added cameras, at the Easton site.

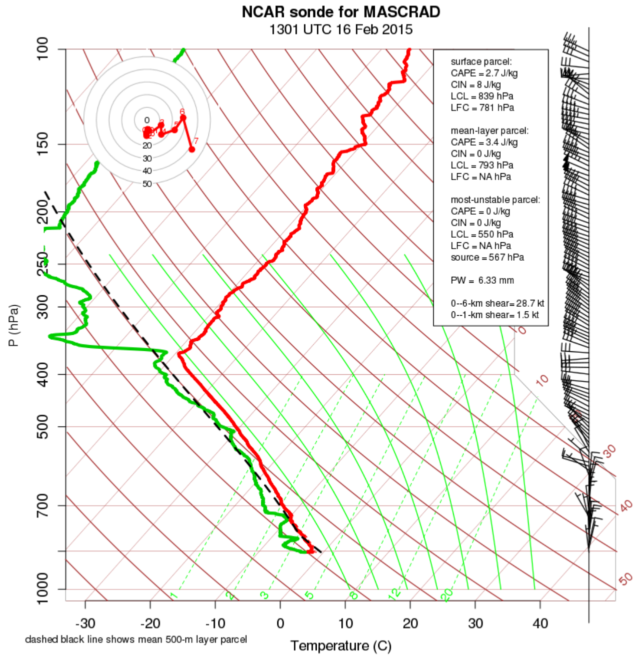

(a)

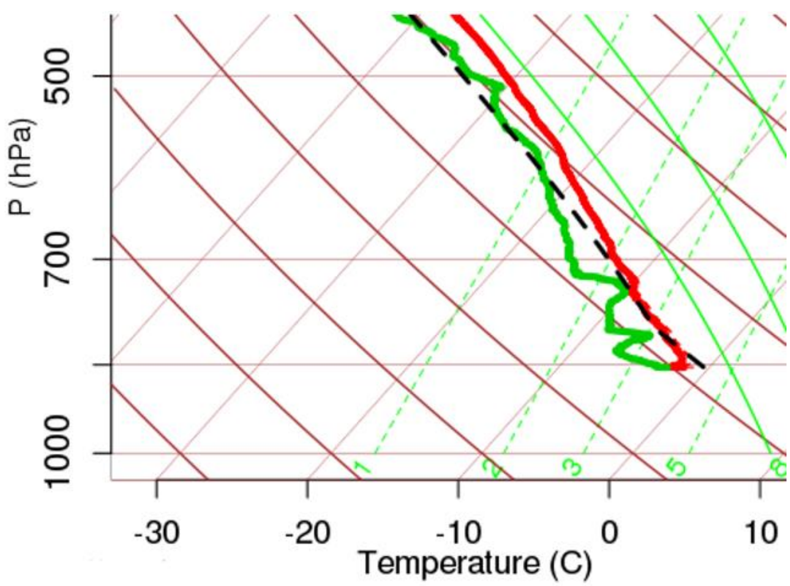

(b)

Figure 4. (a) Skew T-Log P plot of the data launched at 13:01 UTC on 16 February 2015 from the Easton site. Wind speeds plotted in m/s. (b) Magnified view of the lower, graupel shower-bearing, portion of the sounding shown in (a). For reference, the 700 hPa height (-12.5º C) is at 1550 m AGL and the 500 hPa height (-30.6º C) is at 4030 m AGL. The graupel shower echo top height was ~3.5 km AGL (see Figure 11). The sounding temperature at this height was -26º C.

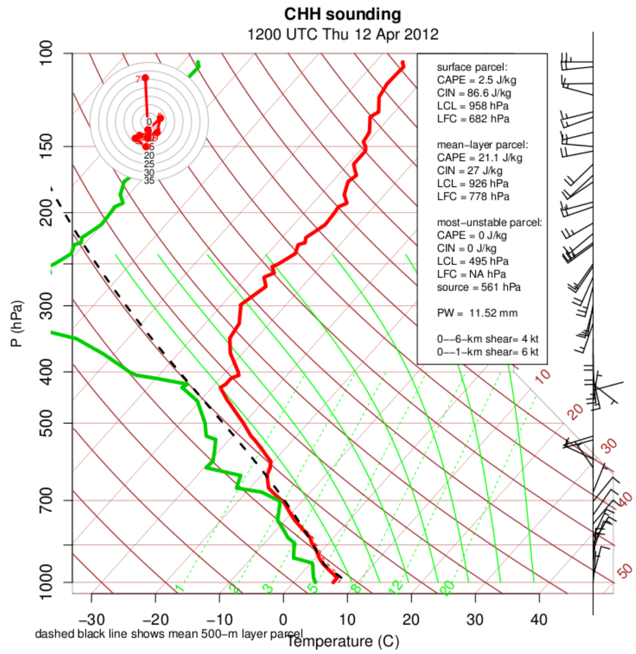

Figure 5. Skew T-Log P plot of the NWS sounding from Chatham, MA at 12 UTC on 12 April 2012. Showers producing small, conical graupel at the surface were observed later on this day (Evaristo et al. 2013).

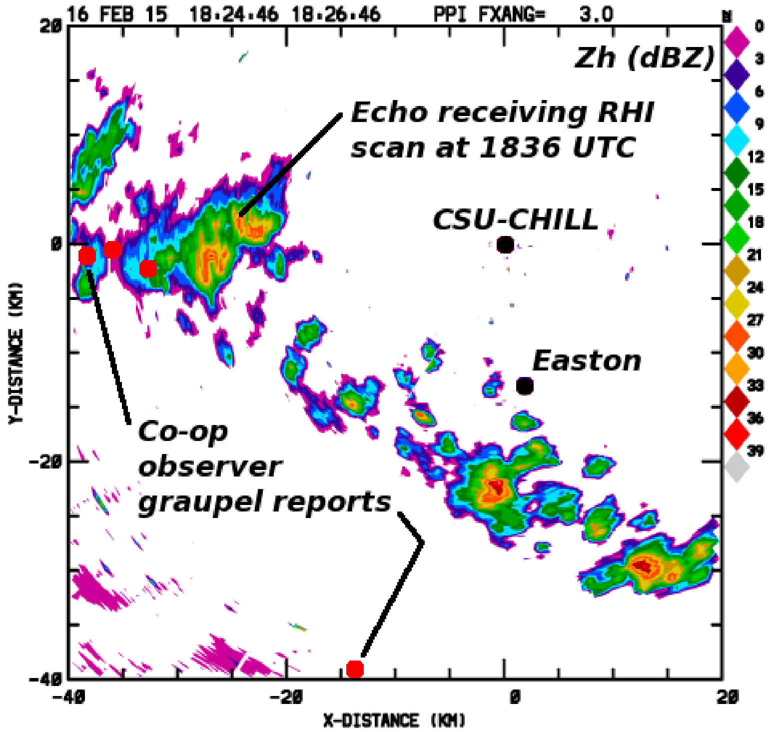

Figure 6. Reflectivity data from the CSU-CHILL radar at 18:24 UTC on 16 February 2015. Elevation angle is 3°; axis labels are in km from an origin at the CSU-CHILL radar.

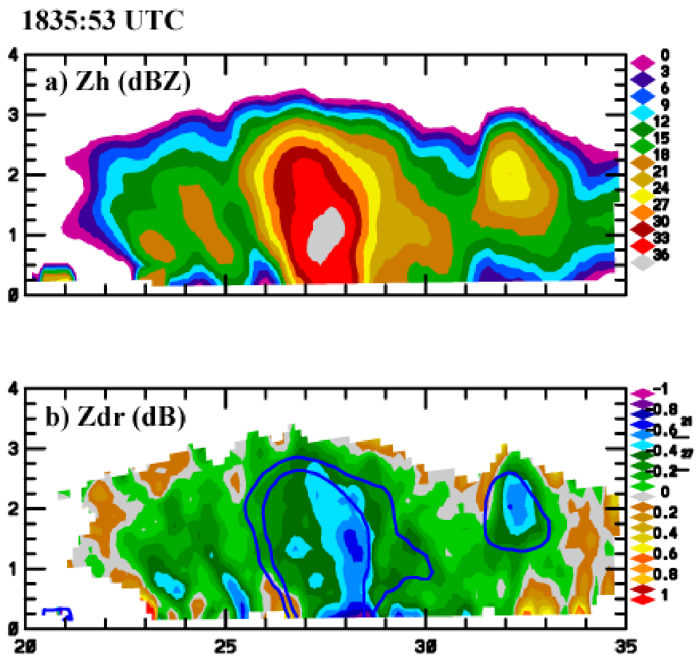

Figure 7. CSU-CHILL RHI scan reflectivity (a) and differential reflectivity (b) data on an azimuth of 261° at 18:35 UTC on 16 February 2015. For reference with panel (a), the solid blue contours in panel (b) are 21 and 27 dBZ.

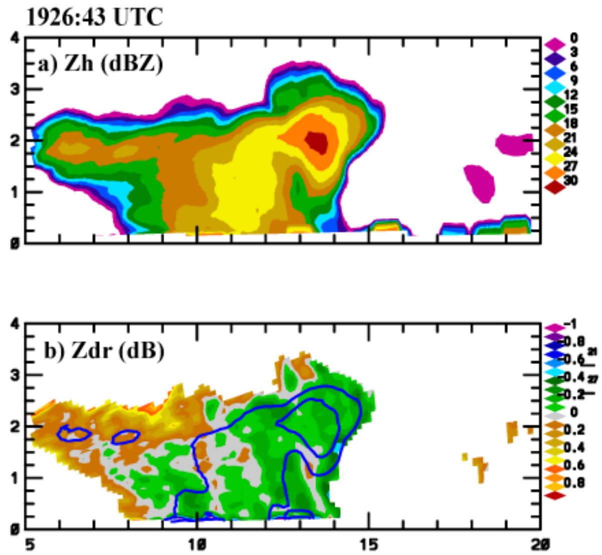

Figure 8. (a) CSU-CHILL RHI scan data taken on the azimuth of the Easton site (171°) at 19:26:43 UTC on 16 February 2015. Easton is located essentially at the 13 km range mark. (a) Z_h in dBZ. (b) Z_{dr} in dB. Solid blue contour lines are 21 and 27 dBZ.

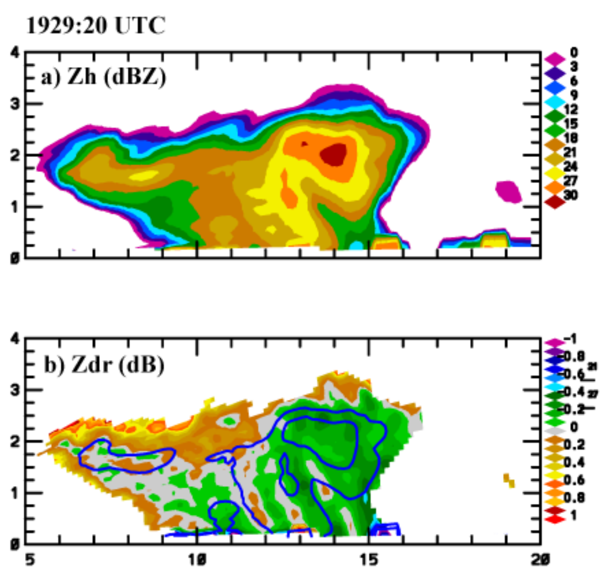

Figure 9. As in Fig. 8 but for the volume start time at 19:29:20 UTC (on 16 February 2015).

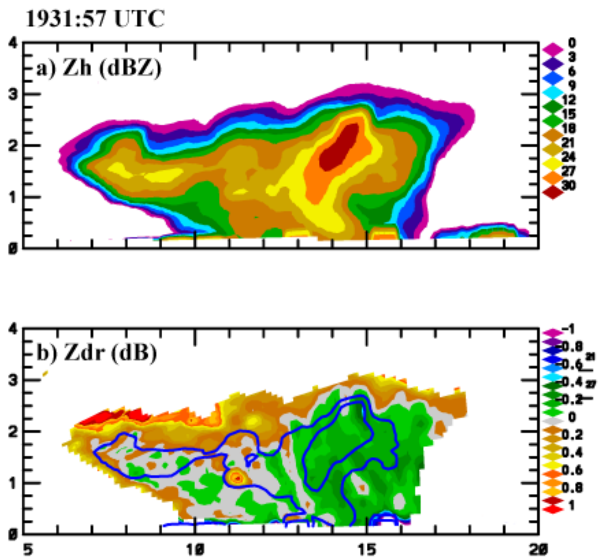

Figure 10. As in Fig. 8 but for the volume start time at 19:31:57 UTC.

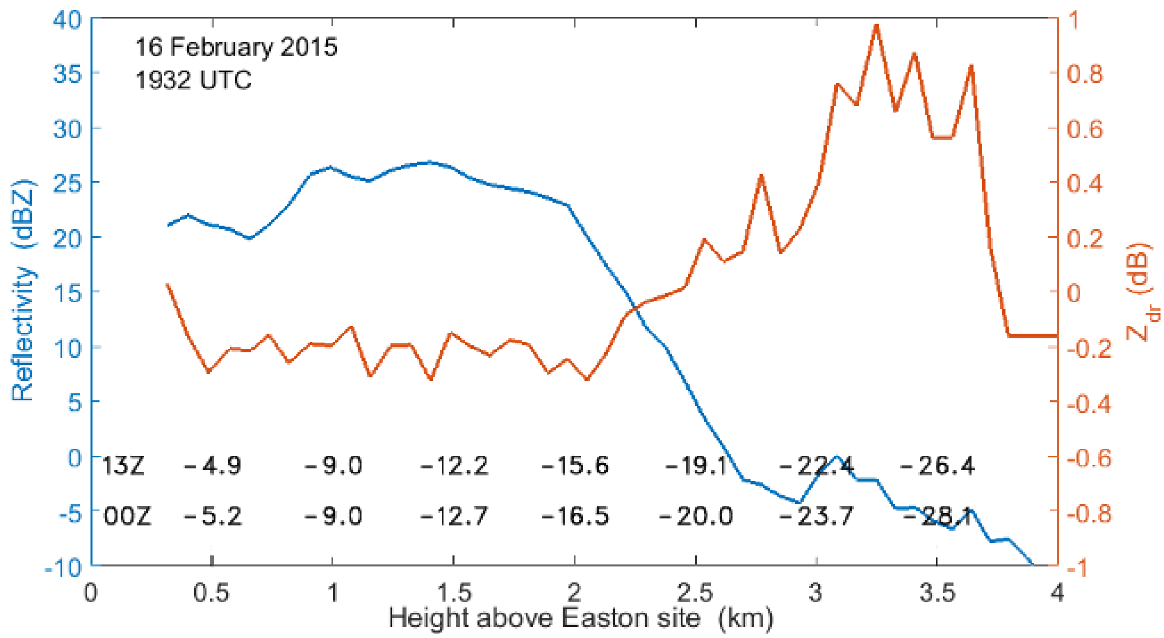

Figure 11. Height profiles of Z_h (blue) and Z_{dr} (red) averaged over a range interval of ± 0.25 km of the Easton site at 19:32 UTC on 16 February 2015. Temperatures (°C) from the 13 UTC Easton sounding are indicated on the abscissa at height intervals of 0.5 km. Temperatures from the 00 UTC NWS Denver sounding are also given. Note that above height of 3.8 km the Z_{dr} data were classified as being due to "non-meteo" echoes and should be disregarded.

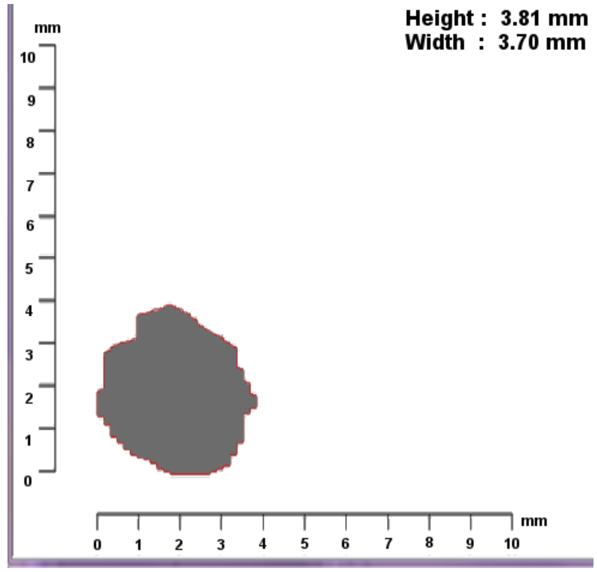

Figure 12. Sample graupel image from one camera of the 2DVD collected at 19:30:08 UTC (on 16 February 2015) at the Easton site. The equi-volume spherical D is 3.5 mm using the images from both cameras. The measured fall speed was 2.6 ms^{-1}.

Figure 13. Sample graupel image from one camera of the MASC (in Fig. 3b) at 19:30:18 UTC. Via 3D reconstruction using five images, the equi-volume spherical *D* is 4.3 mm and fall speed was observed to be 2.6 ms^{-1}.

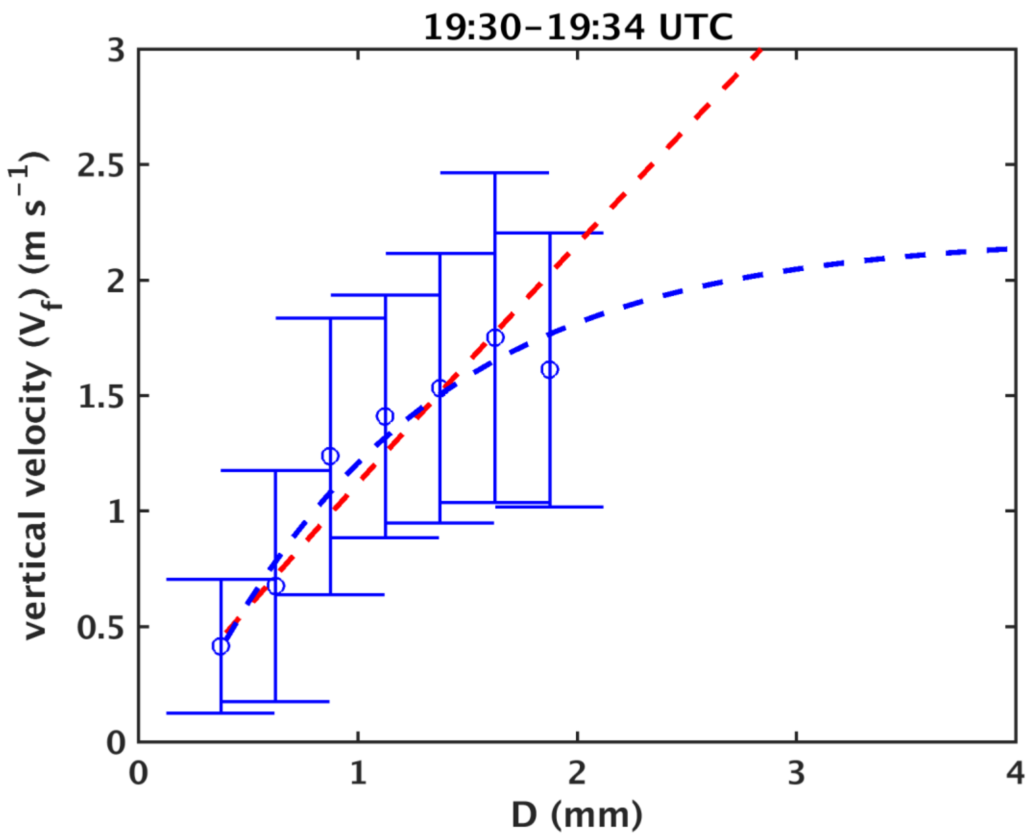

Figure 14. The bin-averaged vertical velocity versus equi-volume diameter (*D*) from the 2DVD for period (i) (19:30-19:34 UTC, on 16 February 2015). The +/− 1σ bars are shown along with an exponential fit (dashed blue line). The power law fit is shown by the dashed red line. The hydrometeors were predominantly small graupel during this time period.

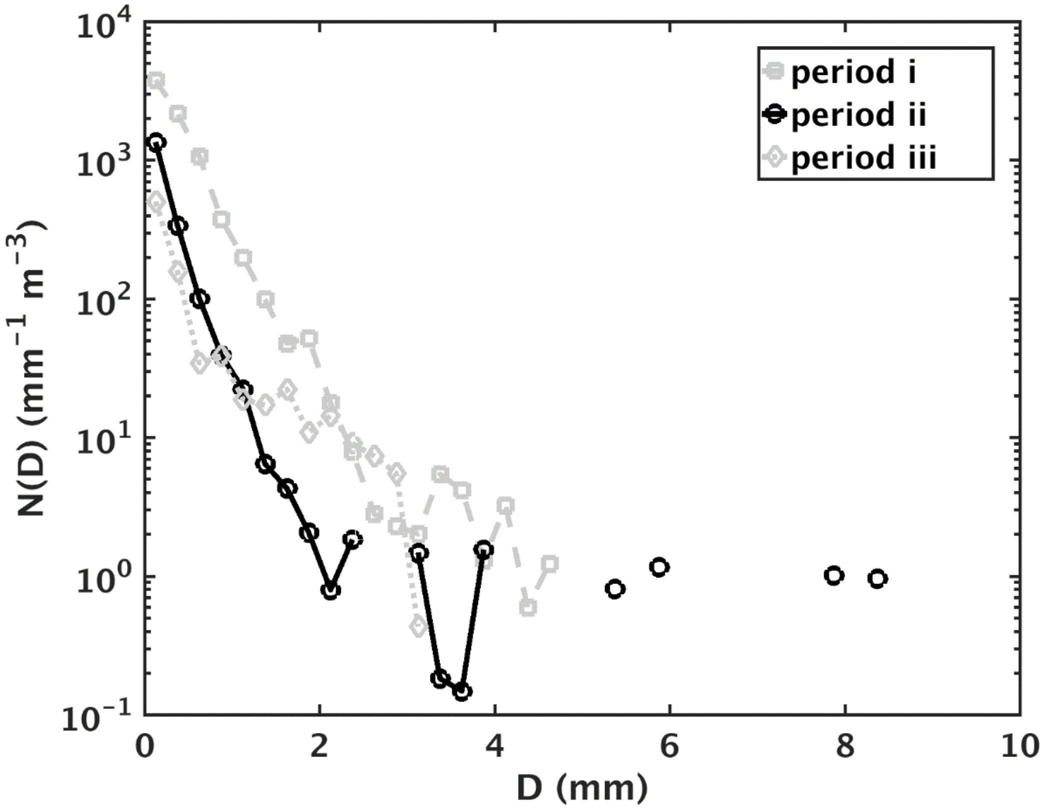

Figure 15. Hydrometeor size distribution *N* versus *D* for the three precipitation shower events. The presence of larger diameter snow aggregates is apparent during period (ii) (plotted in black). The total number of particles sampled during periods (i), (ii) and (iii) were, respectively, 1917, 619 and 513.

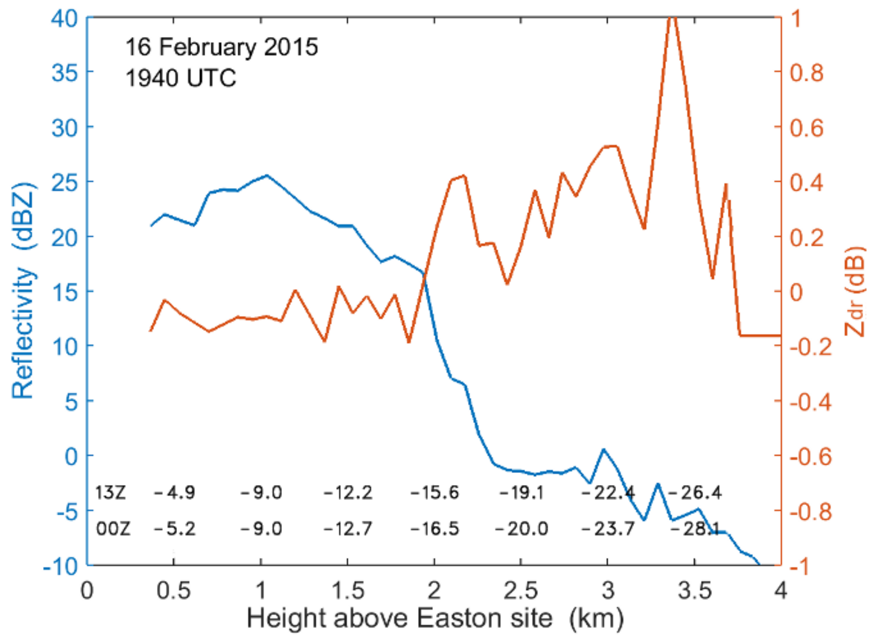

Figure 16. As in Fig. 11 but for 19:40 UTC (shower event period (ii)).

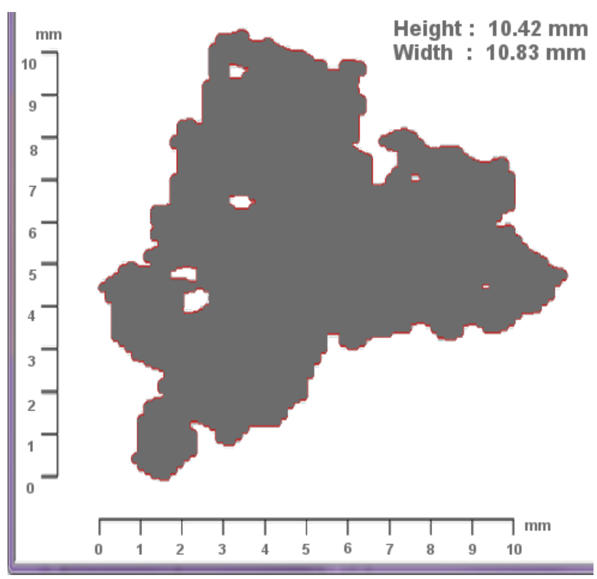

Figure 17. Sample 2DVD image of a large aggregate (D = 8.2 mm; fall speed: 1.3 m^{-1}) at 19:41:24 UTC.

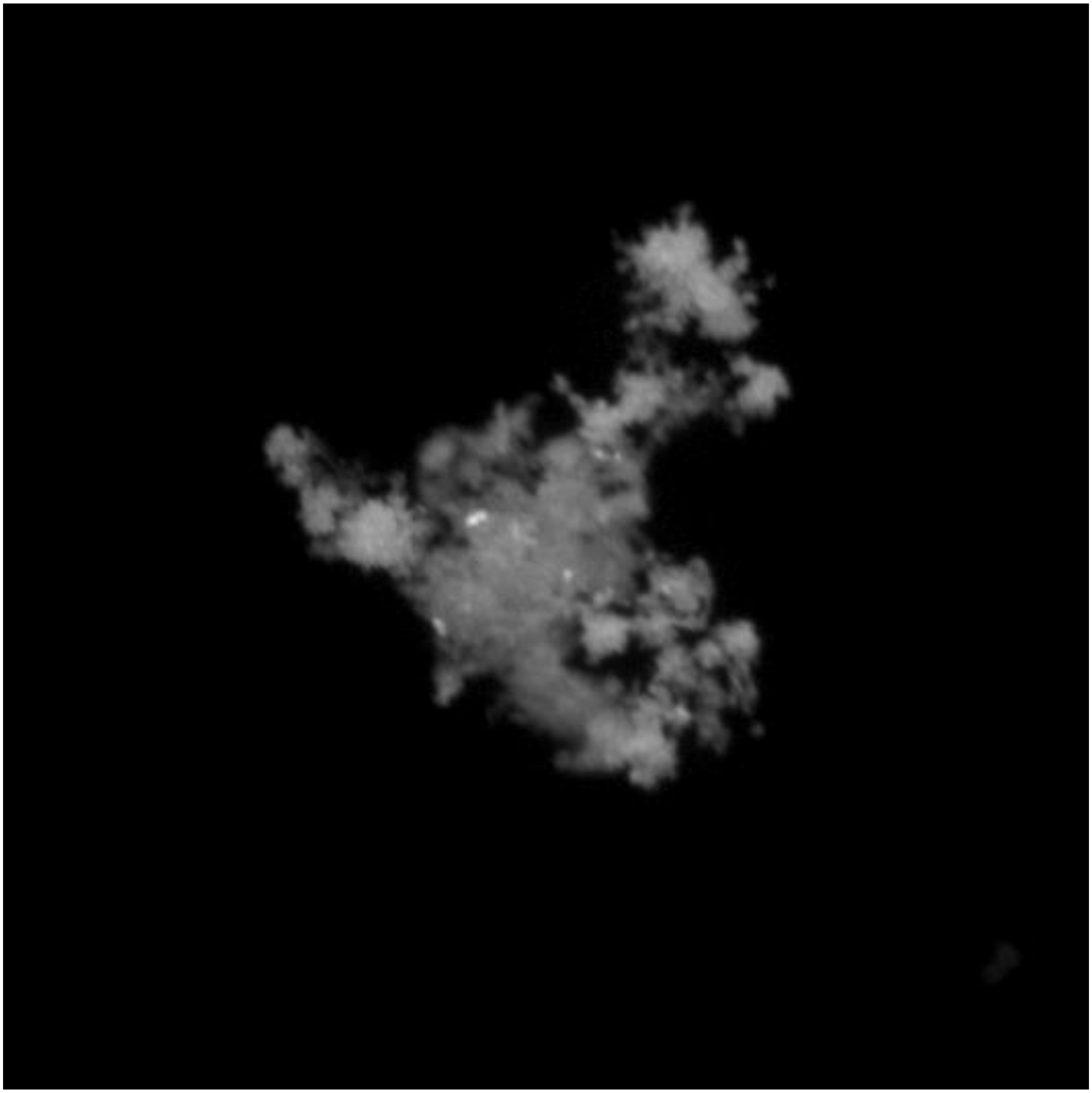

Figure 18. Sample MASC image of a large aggregate (D = 5.6 mm; fall speed: 1.5 ms^{-1}) at 19:41:32 UTC.

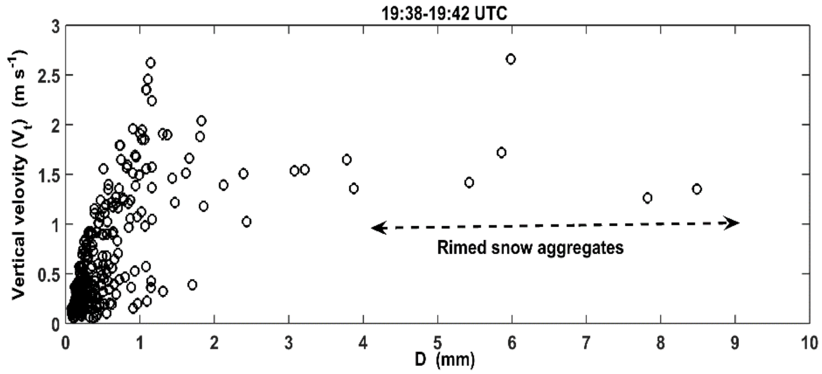

Figure 19. Scatterplot of the vertical velocity versus *D* from the 2DVD for period (ii) (19:38–19:42 UTC).

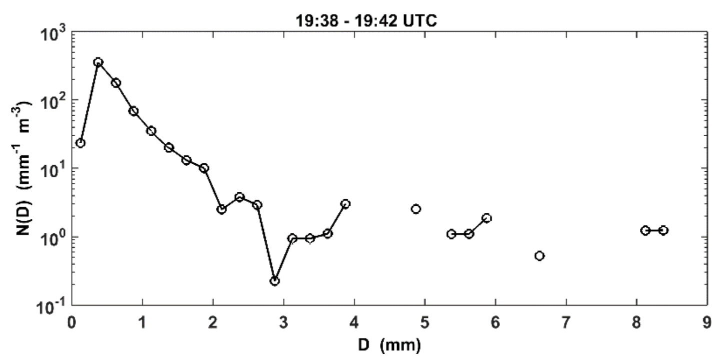

Figure 20. Particle size distribution *N*(*D*) for period (ii).

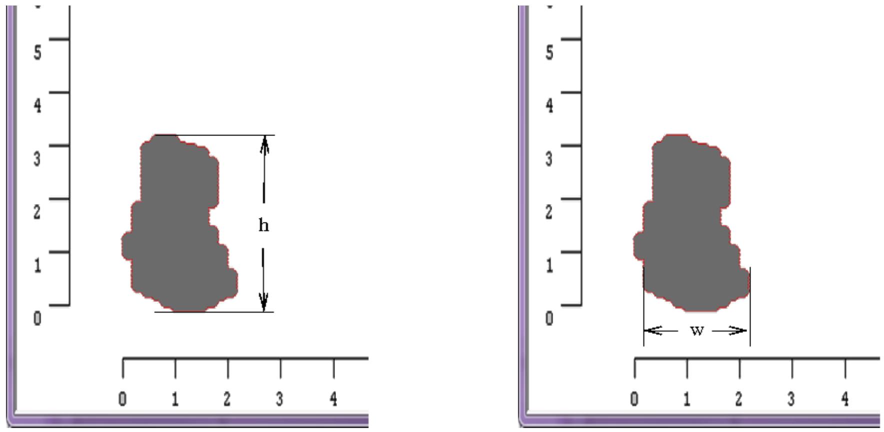

Figure 21. Example of the estimation of height (h) and width (w) from a sample single-camera 2DVD image. The h/w ratio is here loosely referred to as 'axis ratio'.

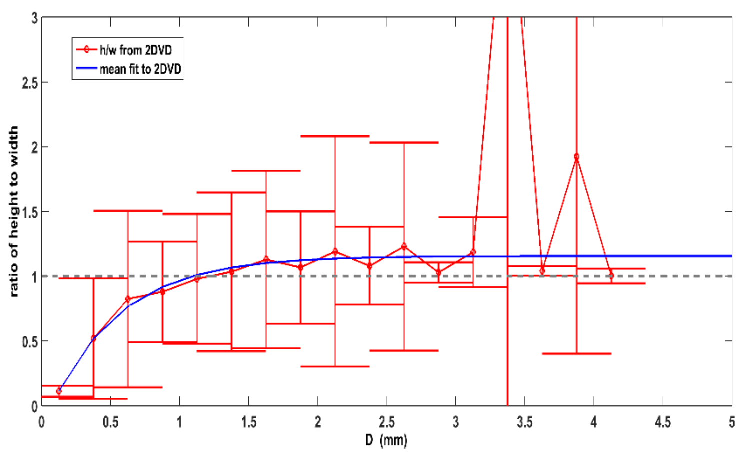

Figure 22. Plot of the bin averaged mean of the height/width versus D from the 2DVD for the entire graupel shower period. Bars depict the +/−1σ extent of the axis ratio values in each diameter bin. Mean fit is shown as blue solid line. Dashed line represents height/width = 1.

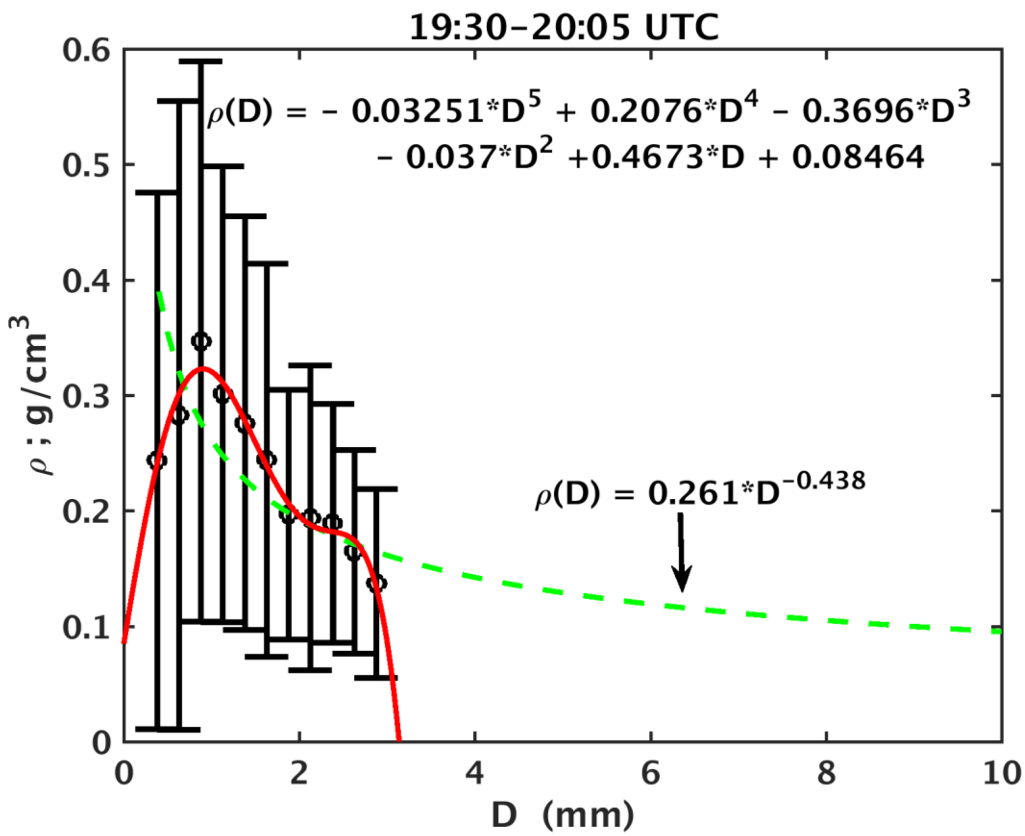

Figure 23. Hydrometeor bulk density vs. diameter for the entire observation period. Vertical bars indicate +/- 1 σ range around the mean value in each diameter bin. Red line is 5th order polynomial fit to the observations: note that we assume $\rho(D>2.875\text{ mm}) = \rho(D=2.875\text{ mm})$ for the polynomial fit. Green dashed line is the indicated power law density vs. diameter relationship.

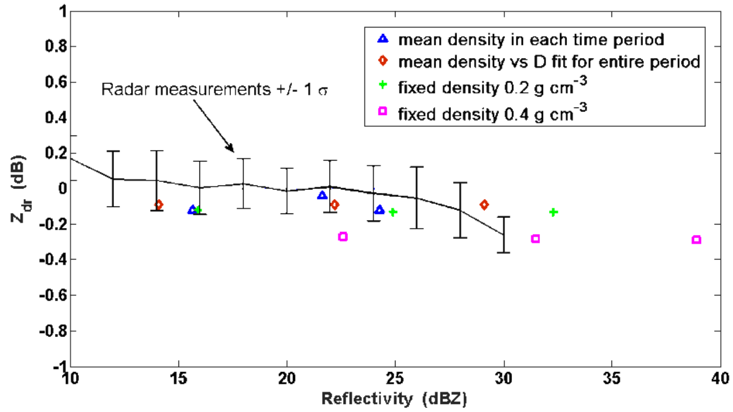

Figure 24. Z_{dr} versus Z_h from radar measurements for all three time periods compared with scattering simulations based on the $N(D)$, mean axis ratio, and density from the 2DVD (various density models are as indicated in the legend). For each density model the lowest, intermediate and largest Z_h correspond, respectively, to periods (iii), (i) and (ii).

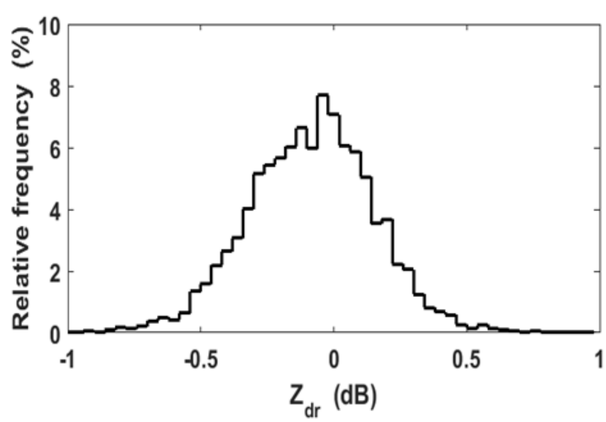

Figure 25. Histogram of radar measured Z_{dr} from all RHI scans over the Easton site from 19:34–20:11 UTC. Data selected from the range interval 10–22 km (range to the Easton site is ~13 km) and height interval 0.5–1.0 km (AGL).

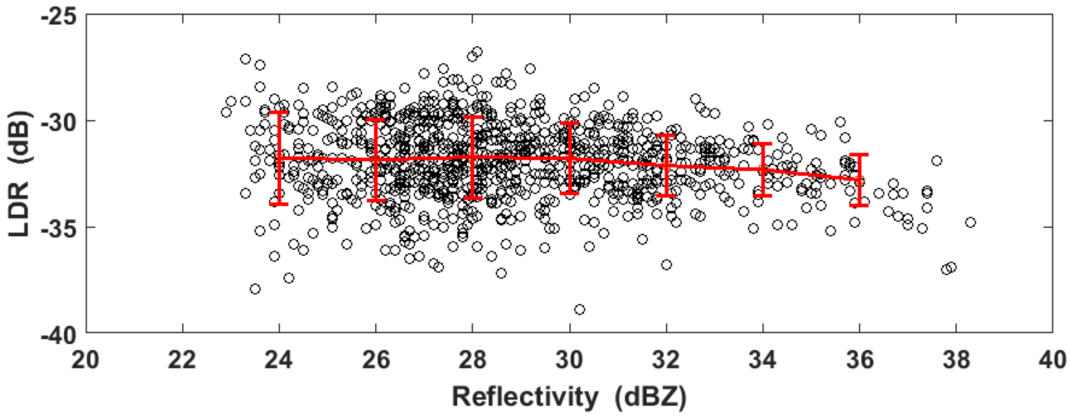

Figure 26. Scatterplot of LDR versus reflectivity radar measurements from RHI scans over Easton. Data selected from the range interval between 10 and 22 km and height interval between 0.5 and 3.0 km (AGL). Bin averaged LDR is also shown along with +/−1σ bars.

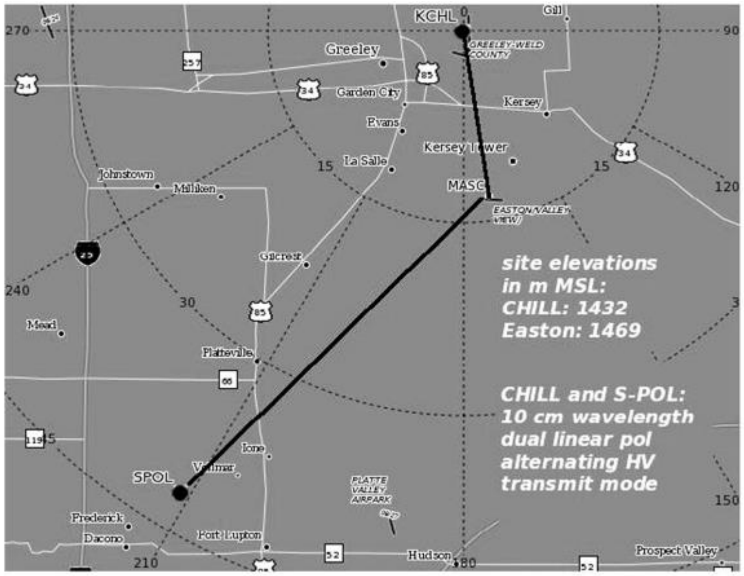

(a)

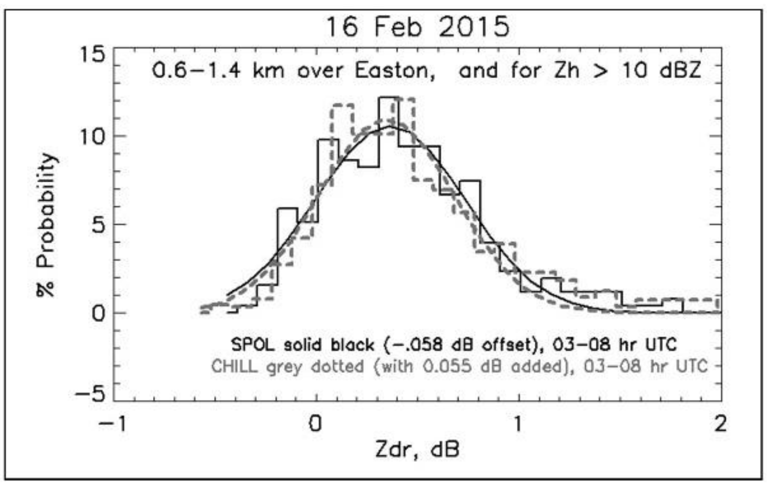

(b)

Figure A1. (a) Depiction of the locations of the CSU-CHILL and NCAR S-Pol radars relative to the Easton instrumentation site. (b) Histograms of Zdr data in the immediate Easton area during widespread snow in the 03 – 08 UTC period on 16 February 2015. S-Pol data plotted in black and CSU-CHILL data in grey.

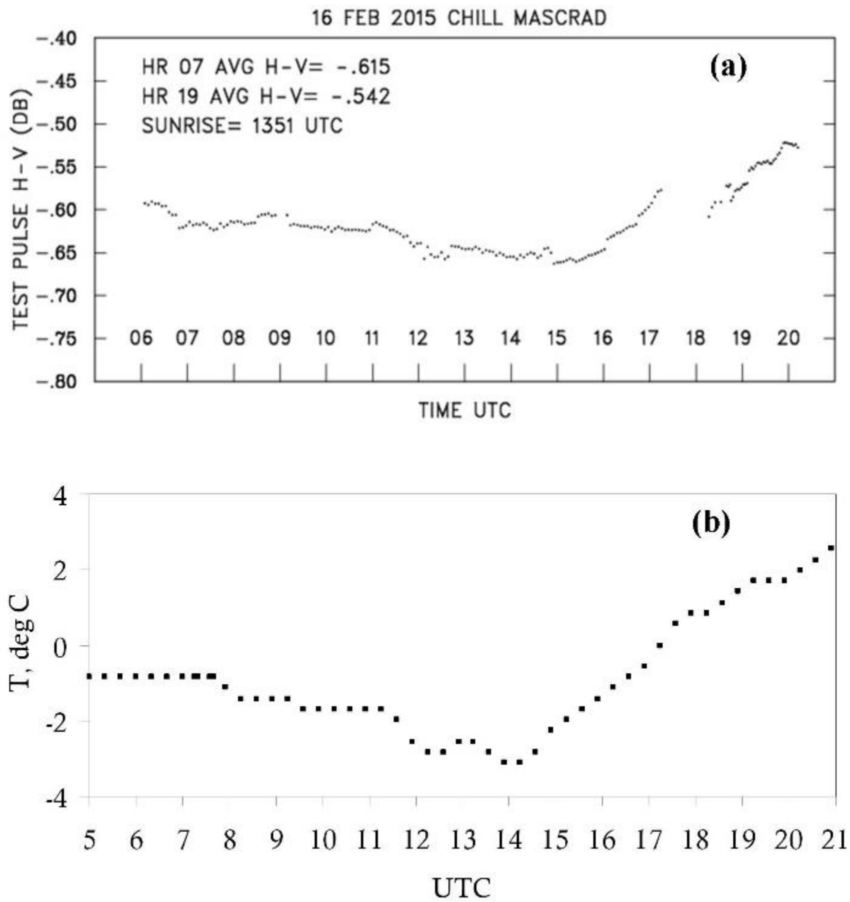

Figure A2. (a) Difference in dB of the test pulse signal levels recorded in the H and V receiver channels of the CSU-CHILL radar as a function of time on 16 February 2015. (Note: The data gap in the 17 – 18 UTC period occurred when the radar was put into standby mode to await echo development). (b) Ambient air temperature measurements for the same time period as recorded at the University of Northern Colorado Earth Science Department. This measurement site is approximately 7 km southwest of the CSU-CHILL radar.